Nano Research

Open Access

Research Article

Interfacial coupling enables high carrier mobility in PbS colloidal quantum dot photodetectors

Qing Li[1], Lier Deng[1] ✉, Yuxuan Du[1], Shasha Chang[1], Shuai Wen[1], Rui Qin[2], Jiuhong Wang[2], Wenzhi Feng[1], Boao Gu[1], and Huan Liu[1] ✉

[1] *Key Laboratory of the Ministry of Education & Thin Film and Optical Manufacturing Technology, School of Opto-Electronic Engineering, Xi'an Technological University, Xi'an 710021, China*
[2] *State Key Laboratory for Manufacturing Systems Engineering, Xi'an Jiaotong University, Xi'an 710049, China*

Cite this article: *Nano Research*, **2025**, *18*, 94907223. https://doi.org/10.26599/NR.2025.94907223

ABSTRACT: Carrier transport in colloidal quantum dot (CQD) films is strongly influenced by the interfacial coupling between CQDs. Currently, the shape of PbS CQDs synthesized using traditional methods results in random orientation relationships between the crystal facets in CQD films, limiting the coupling strength and the final performance of optoelectronic devices. In this study, post-synthesis surface treatment of PbS CQDs was employed to achieve facet control during secondary growth, manipulating the facets of PbS CQDs at the nanoscale to enhance interfacial coupling within CQD films. Additionally, mixed ligands of PbX_2 (X = Br, I) and anhydrous sodium acetate were used to passivate the PbS CQDs, ensuring sufficient passivation. This method combines facet passivation with strong coupling through the (100) facets of CQDs, thereby enhancing carrier mobility and improving device performance. Experimental results showed that, compared to standard PbS CQD films, the electron and hole mobilities of the PbS CQD films subjected to secondary growth were significantly improved, with hole mobility increased by 6 times. Photodetectors fabricated using these films achieved a quantum efficiency of 33% at 1500 nm under 0 V bias, a threefold improvement compared to standard devices.

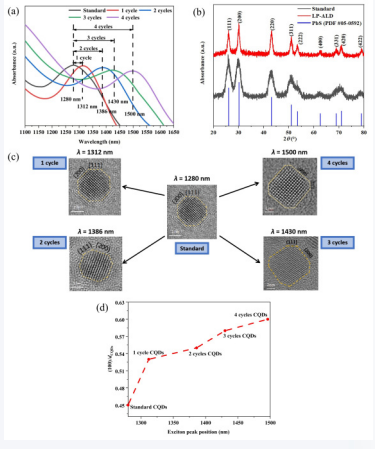

KEYWORDS: interfacial coupling, carrier mobility, liquid-phase atomic layer deposition, liquid-phase ligand exchange, PbS colloidal quantum dot photodetectors

1 Introduction

The coupling of colloidal quantum dots (CQDs) plays a crucial role in carrier transport: Coupling along specific planes can enhance carrier mobility and diffusion length, paving the way for improved performance of CQD optoelectronic devices [1–3]. During device fabrication, short-chain organic or inorganic ligands are essential for enhancing the coupling between quantum dots [4, 5]. Surface ligand exchange has become a significant process for passivating surface defects in CQDs to improve the performance of CQD photodetectors [6]. To address this, Chao Wang et al. [7] optimized the ligand environment of PbS CQDs during synthesis using acetylacetone as a precursor, which avoided the production of water byproducts and reduced surface hydroxyl groups, effectively suppressing non-radiative recombination and enhancing carrier transport in PbS CQD films, thus improving device optoelectronic performance. In 2021, Biondi Margherita et al. [8] developed a colloidal phase reconstruction strategy for CQD surfaces to improve face alignment in CQD films, controlling CQD morphology and enhancing inter-CQD coupling. They utilized a liquid-phase ligand exchange process with traditional PbX_2 (X = Br, I) and anhydrous ammonium acetate, resulting in enhanced optoelectronic performance compared to control CQD devices. However, this liquid-phase mixed ligand passivation strategy was insufficient for adequately passivating CQDs with a high proportion of the (100) crystal face, indicating the need for improvements in traditional ligand exchange to further enhance device performance.

In this study, we employed liquid-phase atomic layer deposition (LP-ALD) to facilitate the rapid growth of quantum dots along the (111) direction, resulting in an increased proportion of the (100) crystal face in PbS CQDs, which is beneficial for enhancing inter-dot coupling. We also utilized mixed ligands of PbX_2 (X = Br, I) and anhydrous sodium acetate for targeted passivation of the PbS

Received: August 14, 2024; **Revised:** December 17, 2024
Accepted: December 25, 2024

✉Address correspondence to Lier Deng, denglier@xatu.edu.cn; Huan Liu, liuhuan360@163.com

CQD crystal faces, thereby improving carrier transport in the quantum dot films. The PbS CQD films treated with LP-ALD exhibited a sixfold increase in hole mobility compared to standard PbS CQD films. Additionally, we fabricated broadband photodetectors with a range of 0.35 to 1.65 μm using PbS CQDs deposited with varying cycle counts. The photodetectors fabricated after four cycles achieved an external quantum efficiency (EQE) of 33% at the first exciton absorption peak, showing significant performance improvements compared to standard devices. Our work confirms that the secondary growth of PbS CQDs via LP-ALD effectively enhances inter-dot coupling in PbS CQD films and improves carrier mobility. The targeted passivation strategy using mixed ligands of PbX_2 (X = Br, I) and anhydrous sodium acetate further enhances device performance.

2 Results and discussion

We performed secondary growth on PbS quantum dots synthesized via a hot injection method using LP-ALD. This process consists of two parts: first, synthesizing PbS quantum dots with an exciton absorption peak around 1280 nm; second, growing the quantum dots using LP-ALD. During this growth process, Pb and S precursors were sequentially added in each cycle, enabling room-temperature secondary growth of the quantum dots. In this method, oleic acid (OA)-capped CQDs were mixed with oleylamine in octane, and an excess of formamide (FA) was introduced as the S^{2-} source. Ammonium sulfide, forming a complex with oleylamine, was transferred to the octane phase. Ammonium sulfide provides protons that strip OA, while S^{2-} preferentially binds to the (111) facets. After rinsing away unreacted precursors, a Pb^{2+} source (lead acetate) was added to the FA. The acetate ions effectively removed harmful hydroxyl (–OH) groups from the quantum dot surfaces, creating an *in-situ* passivation effect. During subsequent ligand treatments, acetate ions were fully replaced by the ligand [8, 9]. The Pb source (lead acetate) added to FA easily transferred to the octane phase and strongly bound to the (111) facets. Pb and S precursors added during this process preferentially bonded with the (111) facets, causing rapid growth along the (111) direction and increasing the surface area of the (100) facets. The *in-situ* passivation with acetate ions during secondary growth effectively reduced interfacial states, and the increased surface area of the (100) facets, due to strong coupling between the (100) facets of PbS CQDs, enhanced the performance of photovoltaic devices [10–12]. To more intuitively demonstrate the secondary growth of PbS CQDs via liquid-phase atomic layer deposition, we conducted a series of optical characterizations on the PbS CQDs before and after deposition. As shown in Fig. 1(a), for each cycle, we observed a red shift in the exciton absorption peak position as the size of the CQDs increased. This is because each additional cycle introduces Pb and S precursors to the existing PbS CQDs, leading to their growth. As the CQDs grow larger in size, their absorption peak shifts to longer wavelengths (red shift). We studied the X-ray diffraction (XRD) spectra of the quantum dots before and after liquid-phase atomic layer deposition to further compare the shape differences in PbS CQDs, as shown in Fig. 1(b). The results confirm that both are single-phase PbS CQDs. Compared to the standard color chart, the PbS CQDs exhibit multiple characteristic diffraction peaks corresponding to the (111), (200), (220), (311), (222), (400), (331), (420), and (422) planes of PbS quantum dots. Additionally, from the XRD spectra, we observed that the primary direction of the PbS CQDs after secondary growth via liquid-phase atomic layer deposition is the (200) XRD peak, whereas the primary direction of the standard PbS CQDs is the (111) XRD peak. This indicates that liquid-phase atomic layer deposition increases the proportion of the (100) facets in PbS CQDs. To better understand how LP-ALD secondary growth affects the shape of PbS CQDs, we performed transmission electron microscopy (TEM) observations on OA-PbS CQDs (oleic acid-capped) before deposition and after different numbers of deposition cycles, as shown in Fig. 1(c). We observed that with increasing cycles, the proportion of the (100) facets also increased. To quantify the shape differences, we compared the (100)/CQD diameter ratio between standard and PbS CQDs with different cycle counts from the TEM images, as illustrated in Fig. 1(d). We found that as the number of cycles increased, the (100)/CQD diameter ratio also increased, indicating a higher proportion of the (100) facets with more deposition cycles.

In the aforementioned study, we performed material characterization of PbS CQDs before and after liquid phase atomic layer deposition (LP-ALD). We analyzed the quantum dots through absorption spectroscopy, TEM, and XRD measurements. To further investigate the impact of liquid phase ALD on the interfacial coupling of the quantum dots, we used standard PbS CQDs and LP-ALD PbS CQDs as light absorption layers in sample devices structured as ITO/electron (hole) transport layer/PbS CQDs (thickness ≈ 300 nm)/electron (hole) transport layer/Au. The device structures are shown in Figs. 2(a) and 2(b), with both the electron (hole) transport layer and the quantum dot layer prepared by spin coating.

Due to the steric hindrance effects of long-chain organic ligands, the film's density is reduced, the electrical coupling between quantum dots is weakened, and the effective carrier transport is hindered [13, 14]. Therefore, surface ligand exchange reactions are essential in the device fabrication process of CQDs. We applied liquid-phase ligand exchange to the device light absorption layer. Liquid-phase ligand exchange provides better passivation of the quantum dot surfaces without organic residues, resulting in fewer surface traps, wider carrier diffusion lengths, and higher mobility [15–17]. Current literature commonly reports using a mixture of PbX_2 (X = Br, I) and anhydrous ammonium acetate dissolved in N,N-dimethylformamide (DMF) solution for liquid-phase ligand exchange with PbS CQDs dissolved in octane. This approach reduces tail states in the bandgap and achieves high-efficiency photovoltaic devices [18]. However, in this method, the ligand exchange of oleic acid with halide lead ions ($[PbX_3]^-$) primarily occurs on the lead-rich polar (111) facets of CQDs, resulting in higher affinity of the anionic ligands with the aid of acidic NH_4^+ cations [15, 18–20]. This method is not suitable for narrow bandgap CQDs with a higher proportion of (100) facets. The oleic acid ligands on the (100) facets are easily removed in polar solvents like DMF. Consequently, the unpassivated (100) surfaces can easily lead to aggregation and precipitation of large-sized PbS CQDs.

To find a more suitable passivation strategy to suppress direct contact on the PbS (100) facets, we first used density functional theory (DFT) to calculate the adsorption energies of halogen atoms and Na atoms on the PbS (100) surface. The adsorption energy is calculated by using Eq. (1)

$$E_{ads} = E_{tot} - E_{slab} - E_i \quad (1)$$

where E_{ads} represents the adsorption energy, E_{tot} is the total energy of the system with the adsorbed atom, E_{slab} is the total energy of the clean slab, and E_i is the energy of the isolated atom. As shown in Fig. 2, the adsorption energies of halogen atoms and Na atoms on

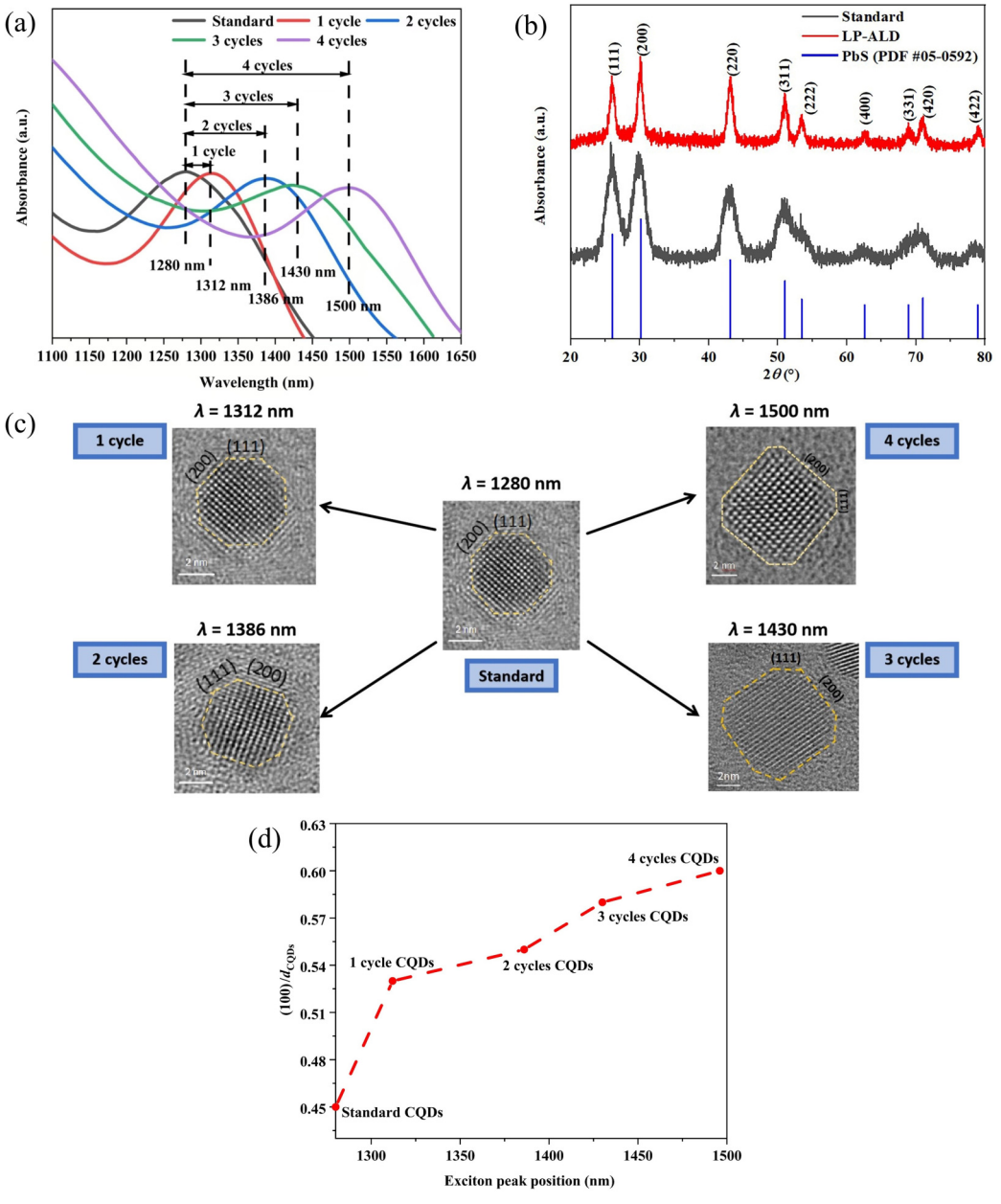

Figure 1 (a) Absorption spectra of PbS CQDs before and after LP-ALD with different numbers of cycles. (b) XRD patterns of standard PbS CQDs and those after different numbers of deposition cycles. (c) TEM images of CQDs before and after different numbers of deposition cycles. (d) The ratio of the (100) crystallographic facet percentage of PbS CQDs to their particle size (dCQDs) at different cycle numbers during liquid-phase atomic layer deposition.

the PbS CQDs (100) surface are all negative, indicating that these atoms can spontaneously adsorb onto the PbS CQDs (100) surface. However, the adsorption energies of Br, Cl, and F atoms are significantly lower than that of I atoms, suggesting that halogens with higher electronegativity can stabilize more effectively on the PbS CQDs (100) surface. Among all halogens, the adsorption energy of Br atoms on the PbS CQDs (100) surface is closest to that of Na atoms. This implies that Na and Br atoms might form a surface passivation layer on the PbS CQDs (100) surface with a nearly stoichiometric ratio. According to Oleksandr Voznyy et al. [21], charge-orbital balance is crucial for controlling the majority carrier types in quantum dot films. Additionally, a stoichiometric ratio would not introduce gap states [22].

We also calculated the surface energy of the system with different coverages of Na-Br atoms adsorbed on the PbS CQDs (100) surface. The calculation method for the surface energy is given by using Eq. (2)

$$E_{surface} = (\Delta H_{tot} - \Delta H_{PbS} - \Delta H_{NaBr})/S_{surface} \quad (2)$$

In this context, $E_{surface}$ represents the surface energy of the system, $S_{surface}$ is the sum of the symmetric upper and lower surfaces. ΔH_{tot} corresponds to the formation enthalpy of the slab model, ΔH_{PbS} is the formation enthalpy of the bulk PbS, and ΔH_{NaBr} is the formation enthalpy of the bulk NaBr. The calculation results of surface energy are shown in Fig. 3. With the increase in the coverage of Na-Br atomic pairs on the PbS CQDs (100) surface, the surface energy generally exhibits a decreasing trend. When the

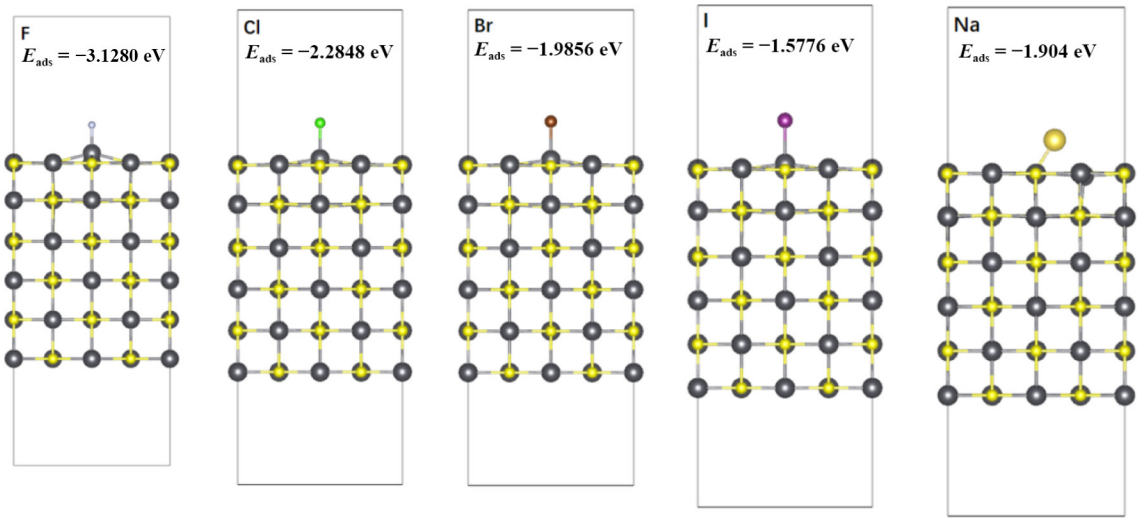

Figure 2 Adsorption energies of halogen atoms and Na atoms on the PbS CQDs (100) surface.

coverage reaches 100%, the surface energy drops to 48.3 meV, indicating that Na-Br atomic pairs effectively passivate the PbS CQDs (100) surface.

Therefore, to achieve better passivation of the (100) plane of PbS CQDs, we employed metal cations and lead bromide to passivate the (100) plane, and lead iodide to passivate the (111) plane during the liquid-phase ligand exchange process. This targeted passivation of different facets provided a higher degree of colloidal stability during and after the liquid-phase ligand exchange. The passivated PbS CQDs exhibited enhanced coupling, reduced inter-dot spacing, and helped suppress the formation of surface defects.

Our goal is to passivate the (100) surface to prevent aggregation of CQDs through the unpassivated (100) surface in polar solvents. X-ray photoelectron spectroscopy (XPS) indicates that the chemical properties of the final CQD film after halide exchange are similar to those of the standard samples and LP-ALD samples (Fig. 4). Due to the surface-specific passivation targeted by different ligands, the proportion of the (100) surface increases while that of the (111) surface decreases. XPS data confirm that the ligand exchange in the liquid phase before and after deposition improves the passivation of the quantum dots.

To investigate the ligand environment on the surface of PbS CQDs films after LP-ALD cycles, Fourier-transform infrared (FTIR) spectroscopy was conducted on the PbS quantum dot films before and after the deposition cycles. The FTIR spectra of the PbS quantum dot films before and after the LP-ALD cycles are shown in Fig. 5. By analyzing the molecular absorption peaks in the FTIR spectra, we confirmed the vibrational characteristics of organic functional groups in the PbS CQDs. Strong vibration peaks corresponding to the C–H(–CH_2) bonds were observed around 2854, 2929 and 2961 cm^{-1}, indicating the presence of oleic acid on the surface of PbS CQDs. The surface treatment of the PbS CQDs after the LP-ALD process still maintains colloidal stability, which is attributed to the oleic acid ligands.

We used the space-charge-limited current (SCLC) method to measure the carrier mobility and trap density of the thin films [23]. In SCLC, carriers drift under the influence of the electric field created by the space charge region, and this drift current is termed the drift current. The current in the space-charge region is constrained by both the carrier charge and the electric field it creates, meaning that the drift current is limited by these two factors [23, 24]. We measured the dark *J*–*V* curve of the fabricated device (device structure shown in Figs. 6(a) and 6(b)). Figures 6(c) and 6(d) depict the current density–voltage relationship curves under SCLC for standard PbS CQD films, while Figs. 6(e) and 6(f) show the current density–voltage relationship curves under SCLC for PbS CQD films deposited via liquid-phase atomic layer deposition. These curves can be roughly divided into three regions. The lower voltage region corresponds to the Ohmic region, where the current is limited by the charge injection capability, and the current-voltage relationship is linear. As the voltage increases, injected carriers accumulate, initiating the filling of semiconductor defect states. The current density undergoes a rapid nonlinear increase, characterizing the trap-filled limit (TFL) region. Partially injected carriers occupy the defect states. The higher voltage region corresponds to the space-charge-limited current (SCLC) regime, where the current is not limited by the charge injection capability but is instead dependent on space-charge limitations. In this regime, the current density is

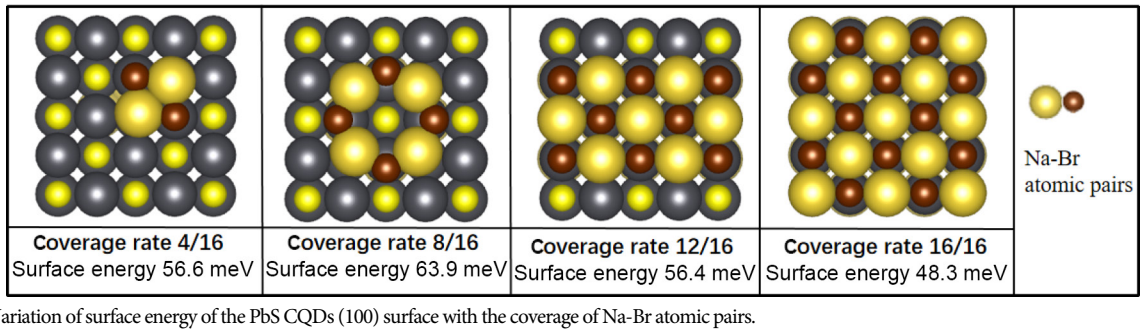

Figure 3 Variation of surface energy of the PbS CQDs (100) surface with the coverage of Na-Br atomic pairs.

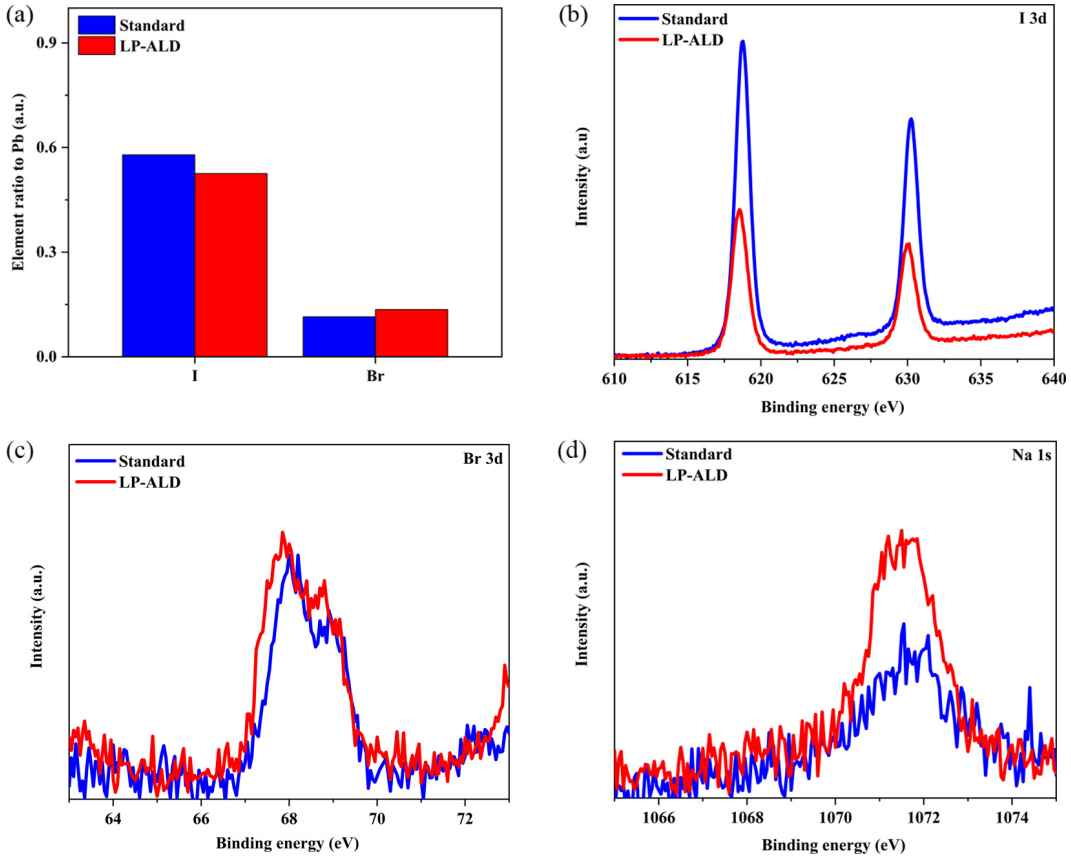

Figure 4 (a) Elemental ratio of lead halides normalized to lead for LP-ALD and Standard PbS CQDs. (b) I 3d, (c) Br 3d, and (d) Na 1s XPS spectra for the liquid-phase ligand exchange films of Standard PbS CQDs and LP-ALD PbS CQDs.

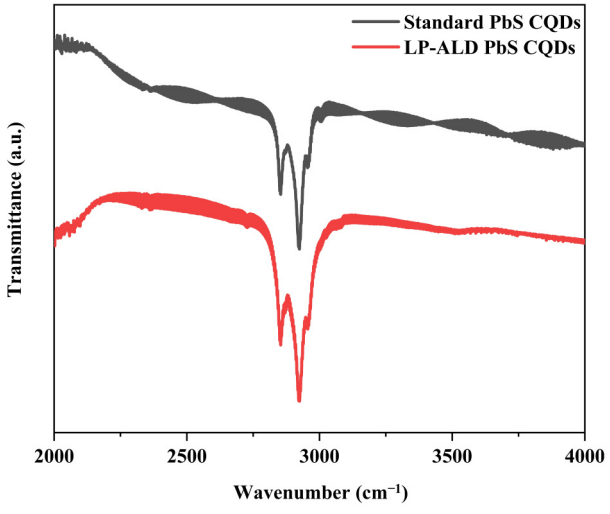

Figure 5 FTIR spectra of PbS CQDs before and after LP-ALD.

proportional to the square of the voltage [25, 26], and the current-voltage relationship is described by Eq. (3) [22, 24–28]

$$J = \frac{9}{8}\frac{\varepsilon\mu}{L^3}V_0^2 \tag{3}$$

where $\varepsilon = \varepsilon_r \cdot \varepsilon_0$, ε_r represents the dielectric constant of the PbS colloidal quantum dot material, with a value of 32, and ε_0 denotes the vacuum permittivity with a value of 8.854×10^{-2} F·m^{-1}. L represents the length of the semiconductor, the thickness of the light-absorbing layer, approximately 300 nm. J denotes the current density flowing through the entire semiconductor, and V is the applied voltage across the semiconductor. μ represents the sought-after mobility. Where $J \propto V^2$, the limit voltage of defect filling V_{TFL} is linearly related to the defect density in the film, as shown in Eq. (4) [25]

$$V_{TFL} = \frac{qN_tL^2}{2\varepsilon_0\varepsilon_r} \tag{4}$$

where L and N_t represent the thickness and defect state density of the PbS CQDs light-absorbing layer film, respectively.

Table 1 summarizes the electrical properties of PbS QD films before and after LP-ALD under dark conditions with a voltage range of 0–5 V. We observed that the PbS CQD films processed with LP-ALD exhibited improved electron and hole mobilities, with the hole mobility increasing by a factor of 6. The density of trap states also decreased. This improvement is attributed to the ability of LP-ALD PbS CQDs to maintain quantum confinement and adequate CQD passivation. The increased proportion of non-polar (100) facets after secondary growth enhances the carrier transport properties of the PbS CQD films due to the strong coupling between (100) facets. Additionally, to demonstrate that the PbS CQDs processed by LP-ALD have fewer trap states, we performed optical characterization of the quantum dots before and after deposition. We tested their fluorescence spectra, as shown in Figs. 7(a) and 7(b). We observed a redshift in the fluorescence spectra relative to the absorption spectra of the quantum dots both before and after deposition. The quantum dots showed a redshift of 74 nm before deposition, and a redshift of 57 nm after LP-ALD treatment. According to the literature [18], the size of the Stokes shift between

Table 1 Comparison of electrical properties of PbS CQD films before and after LP-ALD under dark conditions with 0–5 V voltage

	Electrons			Holes		
	Electron mobility μ_e ($cm^2 \cdot V^{-1} \cdot s^{-1}$)	Trap-filled limit voltage V_{TFL} (V)	Defect state density N_t (cm^{-3})	Hole mobility μ_h ($cm^2 \cdot V^{-1} \cdot s^{-1}$)	Trap-filled limit voltage V_{TFL} (V)	Defect state density N_t (cm^{-3})
Standard PbS CQDs	1.938×10^{-3}	1.61	3.5×10^{15}	1.425×10^{-4}	1.95	5.6×10^{15}
LP-ALD PbS CQDs	2.454×10^{-3}	1.51	2.9×10^{15}	8.991×10^{-4}	1.28	2.4×10^{15}

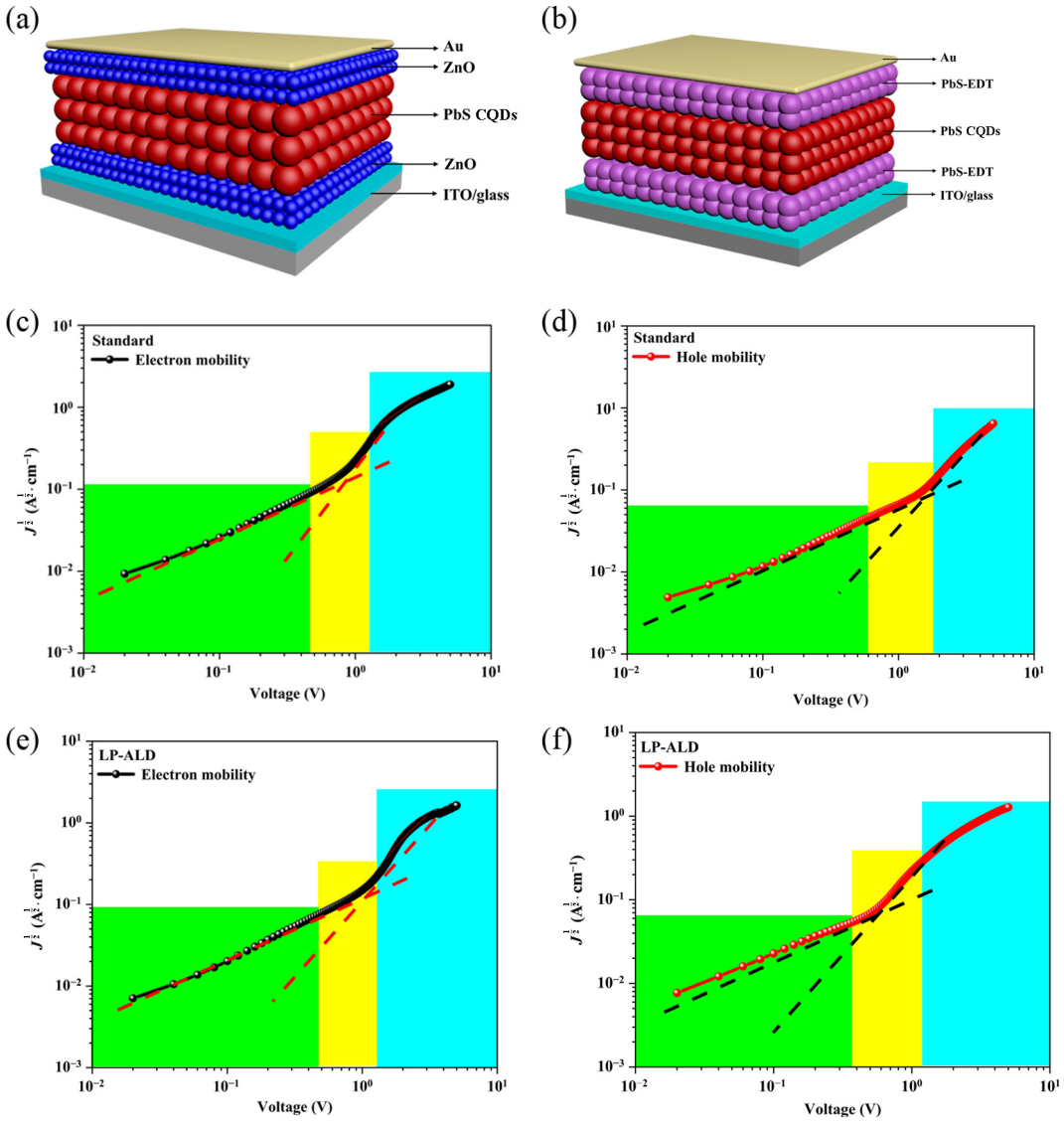

Figure 6 (a) Schematic diagram of the structure of the device for testing electron mobility. (b) Schematic structure of the device for testing hole mobility. (c) Electron mobility (d) hole mobility *J*–*V* curves at 0–5 V in the dark state of a standard PbS colloidal quantum dot films. (e) Electron mobility and (f) hole mobility *J*–*V* curves at 0–5 V in the dark state of PbS colloidal quantum dot films after liquid-phase atomic layer deposition.

the fluorescence and absorption spectra reflects the number of surface defects in the quantum dots. A smaller Stokes shift indicates less defect-related emission in the bandgap, implying better surface passivation and a lower density of surface trap states in the LP-ALD PbS CQDs. The photoluminescence quantum yield (PLQY) of the PbS CQDs after LP-ALD reached 17%, higher than the 13% before deposition. This result also indicates that the PbS CQDs after deposition exhibit better surface passivation and fewer trap states. To further verify the surface defect reduction after LP-ALD treatment, we performed steady-state and transient fluorescence spectroscopy on thin films of the PbS CQDs before and after deposition. This allowed us to study the changes in surface defects between the two types of quantum dots. The steady-state and transient fluorescence spectra of the quantum dots before and after deposition are shown in Fig. 8. We performed biexponential fitting on the transient fluorescence spectra of the quantum dot films before and after deposition, which yielded an average fluorescence lifetime of 0.44 μs for the quantum dot film before deposition, and

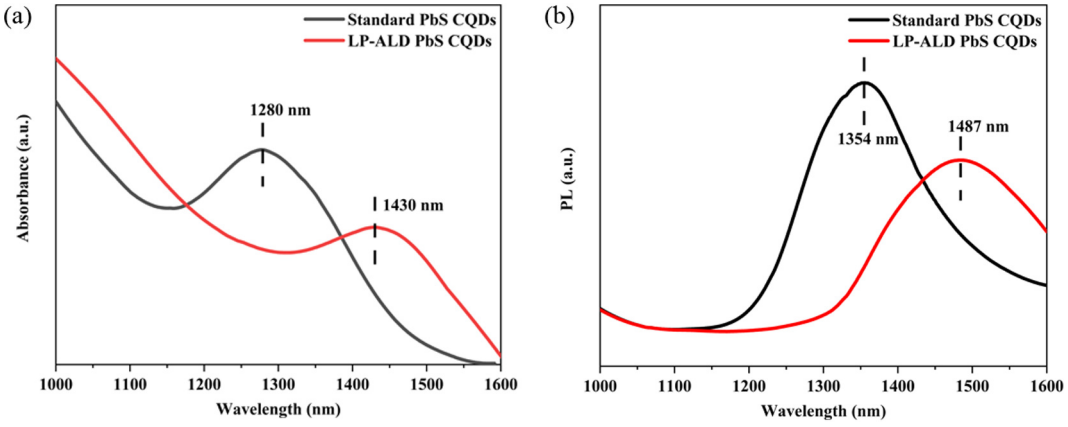

Figure 7 (a) The absorption spectral curves of the colloidal quantum dots before and after deposition. (b) The fluorescence spectral curves of the colloidal quantum dots before and after deposition.

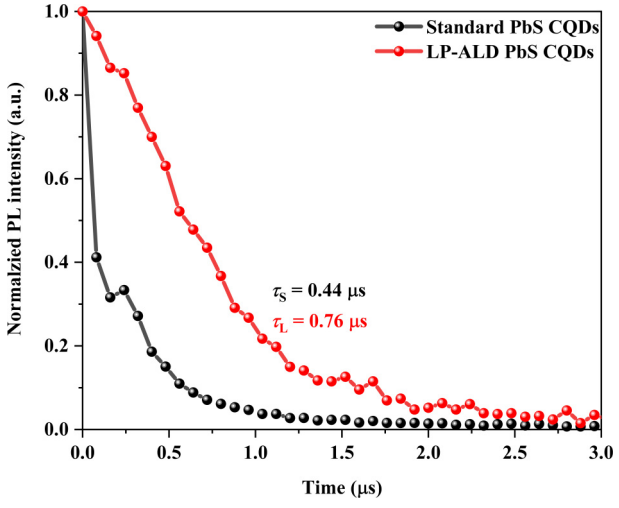

Figure 8 The transient fluorescence decay lifetime spectra of PbS CQDs before and after liquid-phase atomic layer deposition.

0.76 μs for the film after deposition. These fluorescence decay lifetime results confirm that the surface ligands of the PbS CQDs were more completely passivated after LP-ALD treatment, resulting in fewer surface defects. Consequently, this reduces the defect states in the quantum dot film's bandgap and suppresses defect-assisted recombination of photogenerated carriers.

To demonstrate that LP-ALD secondary growth of PbS CQDs can enhance photovoltaic device performance, we prepared photodiode devices with the structure ITO/NiO/PbS-EDT/PbS CQDs/PEIE/ZnO/Al using PbS CQDs with different cycle numbers as the light absorption layer [29]. The light absorption layer was prepared by liquid-phase ligand exchange of PbS CQDs dissolved in n-octane with a mixed ligand solution of PbX_2 (X = Br, I) and anhydrous sodium acetate in N,N-dimethylformamide (DMF). Anhydrous sodium acetate replaced the traditional anhydrous ammonium acetate to ensure sufficient passivation of the PbS CQDs (100) facets. 1,2-Ethanedithiol (EDT)-treated PbS CQDs were used as the p-type hole transport layer, with the NiO layer added to better match the energy levels with the PbS-EDT layer [30]. The ZnO layer served as the electron transport layer, and a thin layer of polyethyleneimine (PEIE) was included to prevent damage to the underlying quantum dots in the light absorption layer [31]. Each layer was fabricated using the spin-coating method, and the device structure is illustrated in Fig. 9(a).

To investigate the optoelectronic performance of the devices, we tested the *I*–*V* characteristic curves of the photodetectors before and after liquid-phase atomic layer deposition over a voltage range of −0.7 to 0.7 V. We found that they exhibited good photovoltaic characteristics, as shown in Fig. 9(b). After deposition, the dark current of the devices decreased while the photocurrent increased. This improvement is attributed to the increased proportion of the PbS CQDs (100) plane after deposition, which enhances the coupling strength between the quantum dots, thereby reducing the dark current. To further quantify the optical performance of the devices, we measured the broadband optical response of PbS CQD devices with different cycle numbers at zero bias voltage, as shown in Fig. 9(c). The EQE represents the device's ability to convert light into electrical current and is defined as the ratio of the number of charge carriers collected to the number of photons incident on the device. The expression for EQE is given in Eq. (5) [32]

$$\mathrm{EQE} = \frac{I_{\mathrm{ph}}/e}{P_{\mathrm{in}}/h\upsilon} = R\frac{hc}{e\lambda} \tag{5}$$

where R is the responsivity of the photodetector, h is Planck's constant, c is the speed of light, λ is the wavelength of incident light, and e is the elementary charge.

We found that the devices exhibited good performance in a self-powered mode both before and after deposition. The EQE of the standard PbS CQD device at its first exciton absorption peak was 10%, while the EQE of the PbS CQD device after liquid-phase atomic layer deposition for secondary growth reached 33%, representing a threefold increase compared to the standard device. The PbS CQD device after four cycles achieved a responsivity (R) of 0.4 $A{\cdot}W^{-1}$ at its first exciton absorption peak, as shown in Fig. 9(d). This improvement is attributed to the increased proportion of the PbS CQDs (100) crystal plane, which enhances strong interactions that alter the hybridization of the electronic orbitals in the quantum dots, leading to band broadening and a reduced bandgap. This, in turn, expands the spectral response range. The combination of lead bromide and anhydrous sodium acetate passivates the (100) crystal plane, resulting in the replacement of long-chain oleic acid ligands in the CQDs, thereby facilitating electron transport and collection. To visually illustrate the trend of EQE and responsivity changes with increasing cycle numbers, we compared the EQE and responsivity values at the first exciton absorption peak for different cycle numbers, as shown in Fig. 9(e). We observed that as the cycle number increased, the EQE of the devices also increased, with

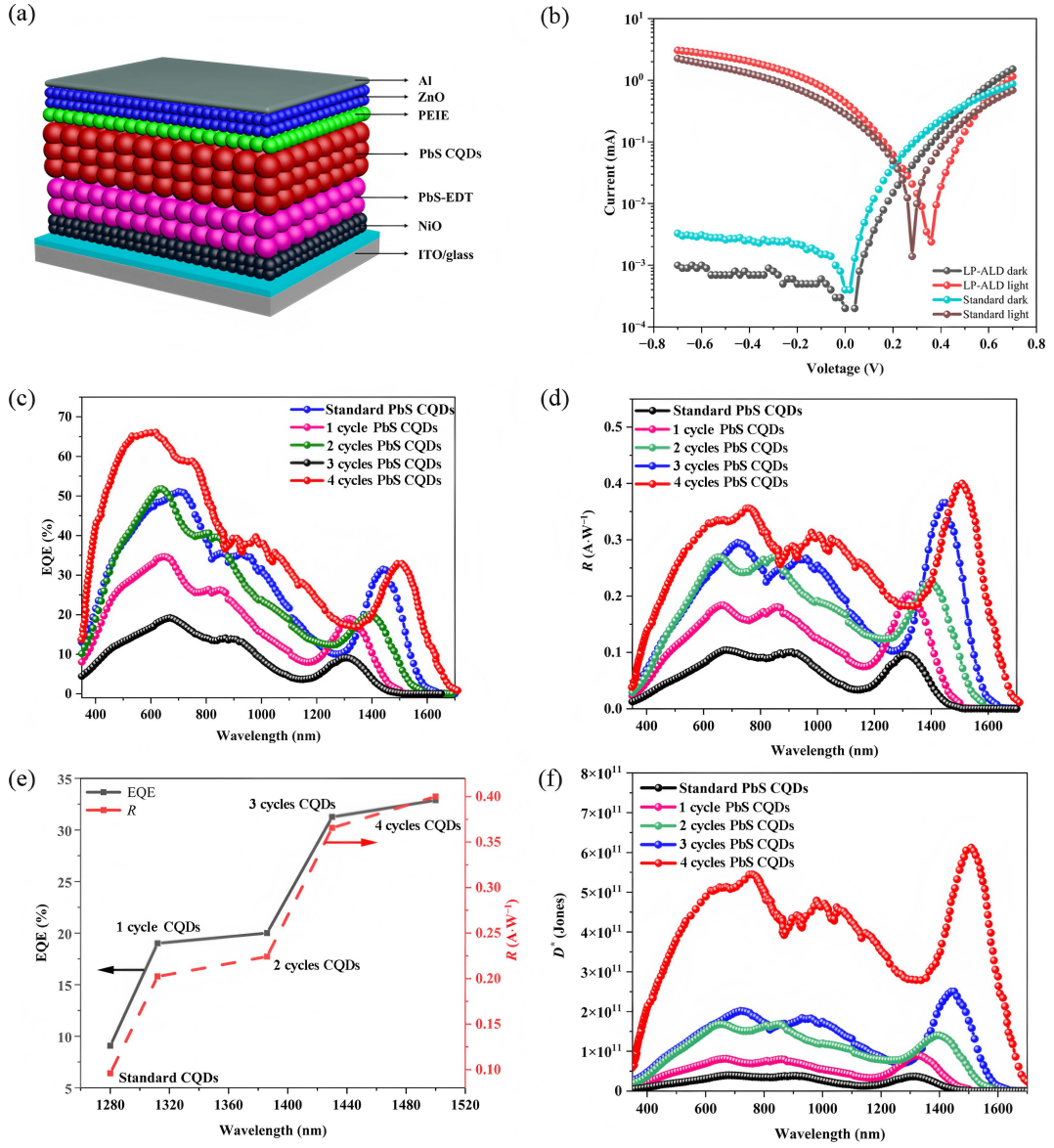

Figure 9 (a) Schematic diagram of the photodetector structure. (b) Current–voltage (*I*–*V*) characteristic curves of the photodetector before and after liquid-phase atomic layer deposition. (c) EQE curves of PbS CQD devices at 0 V bias for different cycling counts. (d) Responsivity curves of PbS CQD devices for different cycling counts. (e) Variation curves of EQE and responsivity with the first exciton absorption peak for different cycling counts. (f) Variation curves of Normalized detection rate with the first exciton absorption peak for different cycling counts.

higher cycle numbers corresponding to larger EQE values. Additionally, the responsivity (*R*) at the first exciton absorption peak also increased with the number of cycles.

The normalized detectivity of PbS quantum dot devices with different cycle numbers is calculated using Eq. (6) [33]

$$D^* = R\sqrt{A}/\sqrt{2eI_{\text{Dark}}} \quad (6)$$

In the equation, *R* represents responsivity, *A* denotes the effective photosensitive area (0.15 cm^2), I_{Dark} is the dark current, and e stands for the elementary charge. Calculations reveal that after four cycle, the normalized detection rate of the device reaches 6.12 × 10^{11} Jones, as shown in Fig. 9(f). This represents a one-order-of-magnitude increase compared to the normalized detection rate of the standard device (3.6 × 10^{10} Jones). This enhancement is attributed to the increased proportion of the (100) surface of PbS CQDs, which allows for adequate passivation of the (100) facets. The coupling strength between the (100) planes is strengthened, improving charge carrier transport and thus enhancing the optoelectronic performance of the device.

To comprehensively evaluate the optoelectronic performance of the devices after liquid-phase atomic layer deposition, we tested various performance parameters of the post-deposition devices. Under 980 nm LED illumination with light power ranging from 30 to 150 mW·cm^{-2}, the current–voltage (*I*–*V*) characteristics of the device are shown in Fig. 10(a), revealing a high rectification ratio exceeding 1500 in the dark at ±0.7 V. Light intensity is a key factor affecting photodetector performance [34]. As the light power varies from 30 to 150 mW·cm^{-2}, the relationship between photocurrent and light intensity is highly dependent on the latter, as illustrated in Fig. 10(b), where the photocurrent shows a linear dependence on light intensity. To investigate the spectral response range of the post-deposition devices, we exposed them to laser irradiation at different wavelengths to test their photoconversion capabilities. The device's

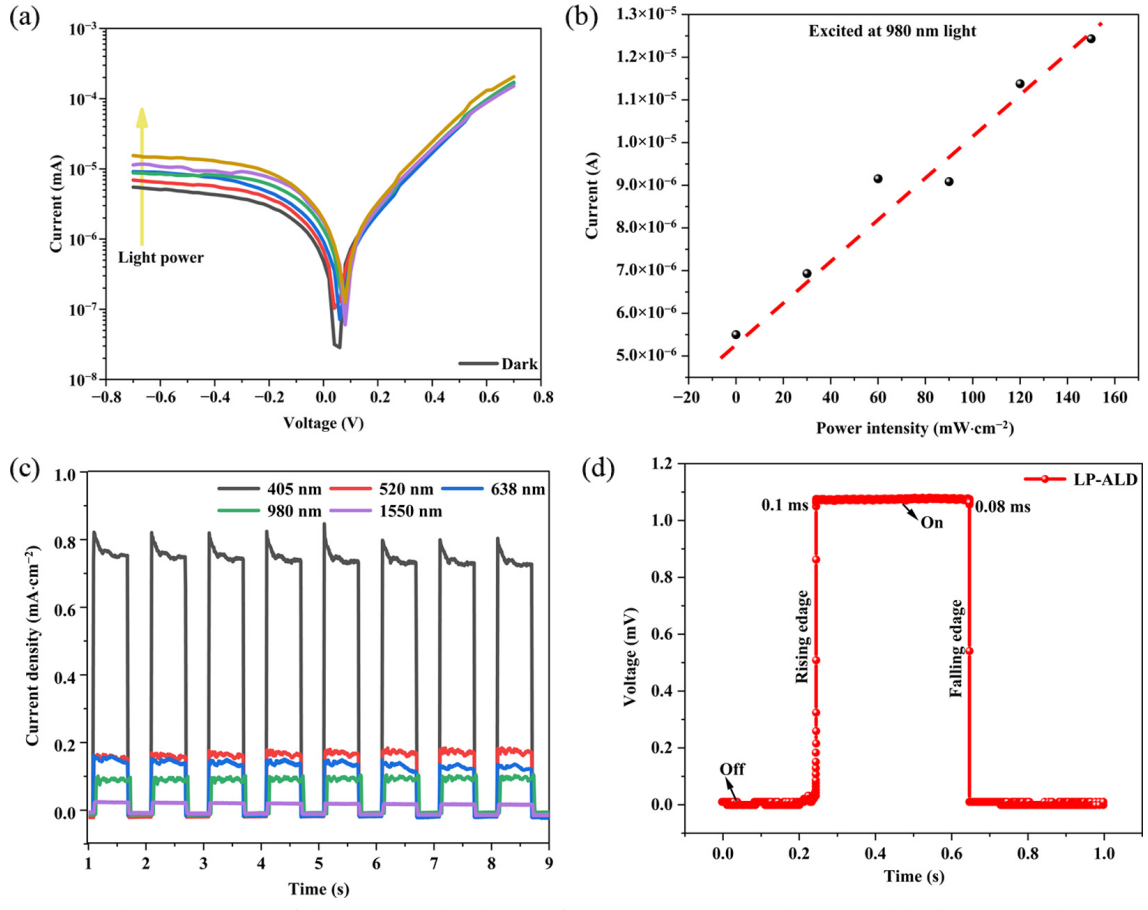

Figure 10 (a) Current–voltage (*I*–*V*) curves of the PbS CQD photodetector after LP-ALD treatment under 980 nm light illumination with power varying from 30 to 150 mW·cm^{-2}. (b) The relationship between photocurrent and light intensity shows a linear dependence as the light power varies from 30 to 150 mW·cm^{-2}. (c) Photoresponse of the device to incident light of different wavelengths, with an incident light intensity of 50 mW·cm^{-2}. (d) Rise and fall curves used to estimate the rise time (τ_r) and fall time (τ_f) of the device.

response to various wavelengths is depicted in Fig. 10(c), demonstrating broad-spectrum detection from visible light (405, 520, and 980 nm) to near-infrared light (980 and 1550 nm) with all illumination powers set at 50 mW. The response time of the photodetector is typically characterized by rise time and fall time. These are defined as the time taken for the signal to rise from 10% to 90% on the response curve and to fall from 90% to 10%, respectively. The response times of the device under illumination are shown in Fig. 10(d). The results indicate that the rise time of the post-deposition device is 0.1 ms and the fall time is 0.08 ms. When the light source is activated, the device responds rapidly due to the generation and diffusion of photo-generated carriers, although it requires longer to traverse these layers before collection at the electrodes. Conversely, when the light source is turned off, the current ceases immediately once the generation of photo-generated carriers stops, resulting in a shorter decay time.

Compared to other studies on PbS CQD devices with similar structures and bandwidths [20, 35, 36], the external quantum efficiency of our photodetector is relatively low, and the response speed is slower. This is primarily because the main objective of this study is to validate the optical and electrical changes of PbS colloidal quantum dots before and after liquid-phase atomic layer deposition. Therefore, the devices were fabricated with only the optical absorption layer parameters altered, without considering factors such as band alignment at the interfaces or the completeness of ligand passivation. If the passivation of the optical absorption layer and the band alignment between the functional layers were optimized through varying deposition cycles [37], there could be further enhancements in the device's photoelectric performance.

3 Conclusions

In this work, we used the LP-ALD method to treat the surface of synthesized PbS CQDs, achieving facet control during secondary growth. This post-synthesis surface treatment method allows for the adjustment of the quantum dot shape, preferentially growing the (100) facets. The strong coupling between the (100) facets enhances the carrier mobility in the colloidal quantum dot films. Targeted passivation of different facets, with the introduction of anhydrous sodium acetate, provides better passivation of the (100) facets, maintaining higher colloidal stability. The hole mobility of the PbS CQD films prepared by this method increased sixfold compared to standard films. Devices exhibited a good response over a wide bandwidth range of 0.35 to 1.65 μm, with an external quantum efficiency of 33% at the first exciton absorption peak under 0V bias, three times higher than standard devices. The responsivity reached 0.4 A·W^{-1}, and the normalized detectivity was 6.12 × 10^{11} Jones. This demonstrates that the post-synthesis surface treatment of PbS CQDs using LP-ALD effectively improves carrier transport performance within quantum dot films. Additionally, the use of mixed ligands of PbX_2 (X = Br, I) and anhydrous sodium acetate for passivating PbS CQDs reduces the density of defect states in

high-performance photodetectors, thereby enhancing device performance.

4 Experiments

4.1 Synthesis of PbS colloidal quantum dots

The synthesis of PbS colloidal quantum dots followed the method reported by Hines et al. [38], with some modifications. To synthesize PbS CQDs with a first excitonic absorption peak at ≈ 1280 nm, 0.45 g of PbO, 1.25 mL of OA, and 18.75 mL of 1-octadecene were mixed in a three-neck flask. The mixture was degassed under vacuum at 120 °C for 1 h to form a clear lead oleate solution. Then, nitrogen gas was introduced into the flask, and the temperature was raised to 135 °C. 210 μL of bis(trimethylsilyl) sulfide (TMS) dissolved in 10 mL of 1-octadecene was rapidly injected into the mixed solution. The color of the solution turned black and was gradually cooled to room temperature. The synthesized solution was transferred to a glovebox, and acetone was added for quenching. Afterward, the solution was washed by adding 3 mL of toluene and vortexing until the quantum dots completely dissolved. Acetone was then added, and this washing step was repeated three times. Finally, the resulting CQDs powder was dissolved in octane (50 mg·L^{-1}). The ratio of PbO, OA, and TMS was adjusted according to the desired final size of the CQDs.

4.2 Liquid-phase atomic layer deposition steps

3 mL of FA, 8 mL of octane, and 100 μL of oleylamine were sequentially added to a centrifuge tube. The tube was hand-shaken and allowed to layer, with FA at the bottom and octane at the top. 0.5 mL of 40% ammonium sulfide aqueous solution and 0.6 mL of PbS CQDs (50 mg·L^{-1} in octane) solution were added to the FA layer. The mixture was vortexed for 1 min, allowed to settle, and then phase-separated (or centrifuged at 1000 rpm for 1 min). The FA solution was removed, and the sample was washed three times with 3 mL of FA, vortexing each time. Then, 3 mL of FA was added, followed by the addition of 0.5 mL of 0.1 mol·L^{-1} lead acetate formamide solution and 100 μL of OA into the FA layer. The mixture was vortexed for 1 min, and then 100 μL of OA was added before centrifugation for layer separation. The FA was removed, washed three times with formamide, and finally, 100 μL of OA was added. This process was repeated, and after completion, 1 mL of OA was added. The mixture was quenched with 15 mL of acetone, washed with toluene, and redispersed in octane (50 mg·L^{-1}).

4.3 Density functional theory (DFT) calculations

For all atom adsorption slab models, structural relaxation and energy calculations were performed using the PBE exchange-correlation functional within DFT. For all halogen atoms, the DZVP pseudopotential basis set was used, combined with the full-electron basis set for Na, and calculated using Gaussian and augmented plane wave (GAPW) methods. Scalar relativistic effects were accounted for using the effective core potentials (GTH). The plane wave cutoff energy was set to 500 Ry. Since local and semi-local functionals cannot account for van der Waals interactions, the Grimme DFT-D3 method was used to correct the Kohn-Sham energy in the calculations. For structural optimization and static self-consistent calculations, the overall energy convergence criterion and the force convergence criterion were set to 5×10^{-6} eV and 3.8×10^{-6} Hartree·bohr^{-1}, respectively. All simulations were conducted in the gas phase at 0 K using the CP2K 2024.1 software package.

4.4 Space charge limited current (SCLC) measurement and sample device fabrication

Dark *J*–*V* characteristic curves were measured for both pure electron devices (ITO/ZnO/PbS CQDs/ZnO/Au) and pure hole devices (ITO/PbS-EDT/PbS CQDs/PbS-EDT/Au) at voltages ranging from 0 to 5 V. The thickness of the PbS CQDs layer was ≈ 300 nm. Fabrication of pure electron devices (ITO/ZnO/PbS CQDs/ZnO/Au):ZnO was dynamically spin-coated on the ITO substrate (5000 rpm, 20 s, 1 layer). PbS colloidal quantum dots, synthesized with a size of ≈ 1280 nm or subjected to secondary growth via liquid-phase atomic layer deposition, were spin-coated at 1800 rpm for 30 s using CQDs ink with a concentration of 300 mg/mL on the ZnO/ITO substrate, resulting in a thickness of ≈ 300 nm. ZnO was dynamically spin-coated on the PbS CQDs/ZnO/ITO substrate (5000 rpm, 20 s, 1 layer). Finally, 80 nm gold electrodes were deposited using thermal evaporation. Fabrication of pure hole devices (ITO/PbS-EDT/PbS CQDs/PbS-EDT/Au) was similar to the fabrication of pure electron devices (ITO/ZnO/PbS CQDs/ZnO/Au), except that the ZnO layer in the device was replaced with a PbS-EDT layer. The PbS-EDT layer was formed by spin-coating PbS colloidal quantum dots at 2500 rpm for 10s, with two layers, resulting in a thickness of ≈ 100 nm. After device fabrication, the mobility in the SCLC system was calculated according to Mott–Gurney's law (*J*–*V*).

4.5 Preparation of PbS CQDs photovoltaic devices

On an ITO substrate, NiO nanoparticles were spin-coated at 2500 rpm for 20 s (1 layer, thickness ≈ 20 nm), followed by annealing at 120 °C for 15 min. The hole transport layer, PbS-EDT layer, was formed by spin-coating PbS colloidal quantum dots at 2500 rpm for 10 s, with two layers, resulting in a thickness of ≈ 100 nm. PbS colloidal quantum dots synthesized with a size of ≈ 1280 nm and those subjected to secondary growth via liquid-phase atomic layer deposition were used at a concentration of 300 mg/mL in CQDs ink, spin-coated at 1800 rpm for 30 s in a mixture of butylamine and dimethylformamide (3:1) on top of the PbS-EDT/NiO/ITO substrate, resulting in a thickness of ≈ 300 nm. Zinc oxide (ZnO) nanoparticles were synthesized using a published method [7]. To prevent damage to the underlying functional layers by ZnO, a layer of polyethyleneimine (PEIE) was spin-coated at 2000 rpm for 20 s on the PbS CQDs/PbS-EDT/NiO/ITO substrate. ZnO was used as the electron transport layer, spin-coated dynamically on the substrate (5000 rpm, 20 s, 1 layer). Aluminum electrodes of 100 nm thickness were deposited using thermal evaporation.

4.6 Characterization

UV–Vis–NIR absorption spectra of PbS colloidal quantum dots were recorded using a UV–Vis–NIR spectrophotometer (HITACHI, U-3501, Tokyo, Japan). The size, crystal facets, and orientations of the quantum dots were determined using transmission electron microscopy (TEM, FEI, Tecnai F20, Lincoln, NE, USA). The crystal structure of the colloidal quantum dots was analyzed using XRD (X'Pert PRO MPD, Nalytical, Holland). The film carrier mobility and device optoelectronic performance were evaluated using an AM0 standard solar simulator testing system (Enlitech, SS-ZXR AM0, Taiwan, China). The quantum efficiency of the devices was measured using a QE-R quantum efficiency testing system (Enlitech, QE-R, Taiwan, China).

Data availability

All data needed to support the conclusions in the paper are presented in the manuscript and the ESM. Additional data related to this paper may be requested from the corresponding author upon request.

Acknowledgements

This research was supported by National Key R&D Program of China (No. 2024YFB3614404), Key Scientific Research Plan of Education Department of Shannxi (No. 23JY035), the National Natural Science Foundation of China (No. 62105256), and Shaanxi Province Natural Science Basic Research Programme (No. 2024JC-YBMS-523).

Declaration of competing interest

All the contributing authors report no conflict of interests in this work.

Author contribution statement

Q. L.: Data curation, project administration, validation, writing manuscript, experimental design. L. E. D.: Project administration, funding acquisition. Y. X. D.: Project administration. S. S. C.: Project administration. S. W.: Project administration, experimental design. R. Q.: Project administration. J. H. W.: Project administration. W. Z. F.: Project administration. B. A. G.: Project administration. H. L.: Funding acquisition. All the authors have approved the final manuscript.

Use of AI statement

None.

References

[1] Tang, J.; Zheng, Y.; Jiang, K.; You, Q.; Yin, Z. T.; Xie, Z. H.; Li, H. N.; Han, C.; Zhang, X. X.; Shi, Y. M. Interlayer exciton dynamics of transition metal dichalcogenide heterostructures under electric fields. *Nano Res.* **2024**, *17*, 4555–4572.

[2] Wu, Z. X.; Ou, Y. D.; Cai, M. Q.; Wang, Y. H.; Tang, R. X. ; Xia, Y. Short‐wave infrared photodetectors and imaging sensors based on lead chalcogenide colloidal quantum dots. *Adv. Opt. Mater.* **2022**, *11*, 2201577.

[3] Zhou, B.; Liu, Z. X.; Fang, S. F.; Zhong, H. Z.; Tian, B. B.; Wang, Y.; Li, H. N.; Hu, H. L.; Shi, Y. M. Efficient white photoluminescence from self-trapped excitons in Sb^{3+}/Bi^{3+}-codoped $Cs_2NaInCl_6$ double perovskites with tunable dual-emission. *ACS Energy Lett.* **2021**, *6*, 3343–3351.

[4] Zhou, B.; Du, A. X.; Ding, D.; Liu, Z. X.; Wang, Y.; Zhong, H. Z.; Li, H. N.; Hu, H. L.; Shi, Y. M. Achieving tunable cold/warm white-light emission in a single perovskite material with near-unity photoluminescence quantum yield. *Nano-Micro Lett.* **2023**, *15*, 207.

[5] Zhao, X. C.; Li, X. M.; Liu, M.; Zhao, Z. J.; Yang, K. X.; Liu, P. T.; Zhang, H. L.; Li, J. T.; Ma, X. L.; Yao, Q. et al. Photomultiplication-type all-polymer photodetectors and their applications in photoplethysmography sensor. *Acta Phys.-Chim. Sin.* **2024**, *41*, 100007.

[6] Zhang, H. L.; Liu, M.; Zhao, X. C.; Ma, X. L.; Yuan, G. C.; Li, J. M.; Zhang, F. J. Photomultiplication type quasi-planar all-polymer photodetectors with tunable response range. *Appl. Phys. Lett.* **2023**, *123*, 111101.

[7] Wang, C.; Wang, Y. L.; Jia, Y. W.; Wang, H.; Li, X. F.; Liu, S.; Liu, X. L.; Zhu, H. B.; Wang, H. Y.; Liu, Y. C. et al. Precursor chemistry enables the surface ligand control of PbS quantum dots for efficient photovoltaics. *Adv. Sci.* **2023**, *10*, 2204655.

[8] Biondi, M.; Choi, M. J.; Wang, Z. B.; Wei, M. Y.; Lee, S.; Choubisa, H.; Sagar, L. K.; Sun, B.; Baek, S. W.; Chen, B. et al. Facet-oriented coupling enables fast and sensitive colloidal quantum dot photodetectors. *Adv. Mater.* **2021**, *33*, 2101056.

[9] Wang, Y. J.; Lu, K. Y.; Han, L.; Liu, Z. K.; Shi, G. Z.; Fang, H. H.; Chen, S.; Wu, T.; Yang, F.; Gu, M. F. et al. *In situ* passivation for efficient PbS quantum dot solar cells by precursor engineering. *Adv. Mater.* **2018**, *30*, 1704871.

[10] Lee, S.; Choi, M. J.; Sharma, G.; Biondi, M.; Chen, B.; Baek, S. W.; Najarian, A. M.; Vafaie, M.; Wicks, J.; Sagar, L. K. et al. Orthogonal colloidal quantum dot inks enable efficient multilayer optoelectronic devices. *Nat. Commun.* **2020**, *11*, 4814.

[11] Choi, M. J.; Kim, Y.; Lim, H.; Alarousu, E.; Adhikari, A.; Shaheen, B. S.; Kim, Y. H.; Mohammed, O. F.; Sargent, E. H.; Kim, J. Y. et al. Tuning solute- redistribution dynamics for scalable fabrication of colloidal quantum-dot optoelectronics. *Adv. Mater.* **2019**, *31*, 1805886.

[12] Zhang, J. B.; Gao, J. B.; Church, C. P.; Miller, E. M.; Luther, J. M.; Klimov, V. I.; Beard, M. C. PbSe quantum dot solar cells with more than 6% efficiency fabricated in ambient atmosphere. *Nano Lett.* **2014**, *14*, 6010–6015.

[13] Kim, Y.; Che, F. L.; Jo, J. W.; Choi, J.; García de Arquer, F. P.; Voznyy, O.; Sun, B.; Kim, J.; Choi, M. J.; Quintero-Bermudez, R. et al. A facet-specific quantum dot passivation strategy for colloid management and efficient infrared photovoltaics. *Adv. Mater.* **2019**, *31*, 1805580.

[14] Fu, J. H.; Min, J. C.; Chang, C. K.; Tseng, C. C.; Wang, Q. X.; Sugisaki, H.; Li, C. Y.; Chang, Y. M.; Alnami, I.; Syong, W. R. et al. Oriented lateral growth of two-dimensional materials on *c*-plane sapphire. *Nat. Nanotechnol.* **2023**, *18*, 1289–1294.

[15] Gan, J.; Yu, M.; Hoye, R. L. Z.; Musselman, K. P.; Li, Y.; Liu, X.; Zheng, Y.; Zu, X.; Li, S.; MacManus-Driscoll, J. L. et al. Defects, photophysics and passivation in Pb-based colloidal quantum dot photovoltaics. *Mater. Today Nano* **2021**, *13*, 100101.

[16] Hu, L.; Lei, Q.; Guan, X. W.; Patterson, R.; Yuan, J. Y.; Lin, C. H.; Kim, J.; Geng, X.; Younis, A.; Wu, X. X. et al. Optimizing surface chemistry of PbS colloidal quantum dot for highly efficient and stable solar cells via chemical binding. *Adv. Sci.* **2021**, *8*, 2003138.

[17] Huang, T. Z.; Wu, C. Y.; Yang, J. P.; Hu, P. Y.; Qian, L.; Sun, T.; Xiang, C. Y. Reducing the open-circuit voltage loss of PbS quantum dot solar cells via hybrid ligand exchange treatment. *ACS Appl. Mater. Interfaces* **2024**, *16*, 915–923.

[18] Xia, Y.; Chen, W.; Zhang, P.; Liu, S. S.; Wang, K.; Yang, X. K.; Tang, H. D.; Lian, L. Y.; He, J. G.; Liu, X. X. et al. Facet control for trap-state suppression in colloidal quantum dot solids. *Adv. Funct. Mater.* **2020**, *30*, 2000594.

[19] Yang, J. R.; Lu, S. C.; Xia, B.; Liu, P. L.; Yang, Y.; Xiao, Z. W.; Zhang, J. B.; Gao, L.; Tang, J. Excess $PbBr_2$ passivation of large PbS colloidal quantum dots to reduce dark-current density for near-infrared detection. *Phys. Rev. Appl.* **2023**, *19*, 014021.

[20] Wang, Y.; Hu, H. C.; Yuan, M. H.; Xia, H.; Zhang, X. C.; Liu, J.; Yang, J.; Xu, S. Q.; Shi, Z. R.; He, J. G. et al. Colloidal PbS quantum dot photodiode imager with suppressed dark current. *ACS Appl. Mater. Interfaces* **2023**, *15*, 58573–58582.

[21] Voznyy, O.; Zhitomirsky, D.; Stadler, P.; Ning, Z. J.; Hoogland, S.; Sargent, E. H. A charge-orbital balance picture of doping in colloidal quantum dot solids. *ACS Nano* **2012**, *6*, 8448–8455.

[22] Kim, D.; Kim, D. H.; Lee, J. H.; Grossman, J. C. Impact of stoichiometry on the electronic structure of PbS quantum dots. *Phys. Rev. Lett.* **2013**, *110*, 196802.

[23] Breen, L. I.; Garner, A. L. Collisional space-charge-limited current with monoenergetic velocity: From child-Langmuir to Mott-gurney.

Phys. Plasmas **2024**, *31*, 032102.
[24] Fang, F. E.; Wan, Y.; Li, H. N.; Fang, S. F.; Huang, F.; Zhou, B.; Jiang, K.; Tung, V.; Li, L. J.; Shi, Y. M. Two-dimensional $Cs_2AgBiBr_6/WS_2$ heterostructure-based photodetector with boosted detectivity via interfacial engineering. *ACS Nano* **2022**, *16*, 3985–3993.
[25] Yu, S. Q.; Xiong, Z.; Zhou, H. T.; Zhang, Q.; Wang, Z. H.; Ma, F.; Qu, Z. H.; Zhao, Y.; Chu, X. B.; Zhang, X. W. et al. Homogenized NiO_x nanoparticles for improved hole transport in inverted perovskite solar cells. *Science* **2023**, *382*, 1399–1404.
[26] Zhang, L.; Chen, Y.; Cao, S.; Yuan, D. F.; Tang, X.; Wang, D. K.; Gao, Y. J.; Zhang, J. J.; Zhao, Y. B.; Yang, X. C. et al. Interfacial heterojunction enables high efficient PbS quantum dot solar cells. *Adv. Sci.* **2024**, *11*, 2402756.
[27] Sun, B.; Vafaie, M.; Levina, L.; Wei, M. Y.; Dong, Y. T.; Gao, Y. J.; Kung, H. T.; Biondi, M.; Proppe, A. H.; Chen, B. et al. Ligand-assisted reconstruction of colloidal quantum dots decreases trap state density. *Nano Lett.* **2020**, *20*, 3694–3702.
[28] Ding, C.; Liu, F.; Zhang, Y. H.; Hayase, S.; Masuda, T.; Wang, R. X.; Zhou, Y.; Yao, Y. F.; Zou, Z. G.; Shen, Q. Passivation strategy of reducing both electron and hole trap states for achieving high-efficiency PbS quantum-dot solar cells with power conversion efficiency over 12%. *ACS Energy Lett.* **2020**, *5*, 3224–3236.
[29] Goossens, V. M.; Sukharevska, N. V.; Dirin, D. N.; Kovalenko, M. V.; Loi, M. A. Scalable fabrication of efficient p-n junction lead sulfide quantum dot solar cells. *Cell Rep. Phys. Sci.* **2021**, *2*, 100655.
[30] Ding, C.; Wang, D. D.; Liu, D.; Li, H.; Li, Y. S.; Hayase, S.; Sogabe, T.; Masuda, T.; Zhou, Y.; Yao, Y. F. et al. Over 15% efficiency PbS quantum-dot solar cells by synergistic effects of three interface engineering: Reducing nonradiative recombination and balancing charge carrier extraction. *Adv. Energy Mater.* **2022**, *12*, 2201676.
[31] Zhang, Y. H.; Wu, G. H.; Liu, F.; Ding, C.; Zou, Z. G.; Shen, Q. Photoexcited carrier dynamics in colloidal quantum dot solar cells: Insights into individual quantum dots, quantum dot solid films and devices. *Chem. Soc. Rev.* **2020**, *49*, 49–84.
[32] Xiao, G. N.; Liang, T. H.; Wang, X. M.; Ying, C.; Lv, K.; Shi, C. W. Reduced surface trap states of PbS quantum dots by acetonitrile treatment for efficient SnO_2-based PbS quantum dot solar cells. *ACS Omega* **2024**, *9*, 12211–12218.
[33] Mao, C. H.; Dubey, A.; Lee, F. J.; Chen, C. Y.; Tang, S. Y.; Ranjan, A.; Lu, M. Y.; Chueh, Y. L.; Gwo, S.; Yen, T. J. An ultrasensitive gateless photodetector based on the 2D bilayer MoS_2-1D Si nanowire-0D Ag nanoparticle hybrid structure. *ACS Appl. Mater. Interfaces* **2021**, *13*, 4126–4132.
[34] Fu, Y. J.; Wang, Y. J.; Zhao, J. J.; Wen, S.; Liu, H.; Li, Q.; Gu, B. A.; Deng, L. E. Size-tunable and monodisperse lead sulfide quantum dots for broadband photodetectors. *APL Mater.* **2024**, *12*, 031126.
[35] Zhang, L. X.; Chen, L.; Yang, J. R.; Liu, J.; Lu, S. C.; Liang, X. Y.; Zhao, X. Z.; Yang, Y.; Hu, J.; Hu, L. et al. High-performance and stable colloidal quantum dots imager via energy band engineering. *Nano Lett.* **2023**, *23*, 6489–6496.
[36] Liu, J.; Liu, P. L.; Chen, D. Y.; Shi, T. L.; Qu, X. X.; Chen, L.; Wu, T.; Ke, J. P.; Xiong, K.; Li, M. Y. et al. A near-infrared colloidal quantum dot imager with monolithically integrated readout circuitry. *Nat. Electron.* **2022**, *5*, 443–451.
[37] Lu, S. C.; Liu, P. L.; Yang, J. R.; Liu, S. J.; Yang, Y.; Chen, L.; Liu, J.; Liu, Y. X.; Wang, B.; Lan, X. Z. et al. High-performance colloidal quantum dot photodiodes via suppressing interface defects. *ACS Appl. Mater. Interfaces* **2023**, *15*, 12061–12069.
[38] Hines, M. A.; Scholes, G. D. Colloidal PbS nanocrystals with size-tunable near-infrared emission: Observation of post-synthesis self-narrowing of the particle size distribution. *Adv. Mater.* **2003**, *15*, 1844–1849.